instruments

MDPI

Article

Feasibility Study of a PET Detector with a Wavelength-Shifting Fiber Readout

Anzori Sh. Georgadze [1,2]

[1] Institute of Physics, Tartu University, W. Ostwaldi 1, 50411 Tartu, Estonia; anzori.heorhadze@ut.ee
[2] Institute for Nuclear Research, National Academy of Sciences of Ukraine, Prospekt Nauky 47, 03680 Kyiv, Ukraine

Abstract: We designed and evaluated the performance of a high-resolution large-area detector for positron emission tomography (PET) based on a crystal assembly readout using wavelength-shifting (WLS) fibers, offering a cost-effective alternative to the direct readout of monolithic crystals with photodetectors. The considered detector geometries were made up of 4 × 4 assemblies of LuY_2SiO_5:Ce (LYSO) crystal scintillators, each with surface area of 50 × 50 mm^2 and thickness of 7 or 15 mm, which were optically coupled together using optical adhesive. The crystal assembly was coupled with square cross-sections of orthogonal wavelength-shifting (WLS) fibers placed on the top and bottom of the assembly. To evaluate the characteristics of the novel detector, we used GEANT4 to perform optical photon transport in the crystal assembly and WLS fibers. The simulation results show that best position resolution achieved was 1.6 ± 0.4 mm full width at half maximum (FWHM) and 4.2 ± 0.6 mm full width at tenth maximum (FWTM) for the crystal thickness of 7 mm and 1.7 ± 0.4 mm FWHM and 6.0 ± 0.6 mm FWTM for the crystal thickness of 15 mm. Compared with a direct photosensor readout, WLS fibers can drastically reduce the number of photosensors required while covering a larger sensitive detection area. In the proposed detector design, 2N photodetectors are used to cover the same image area instead of N^2 with a direct readout. This design allows for the development of a compact detector with an expanded effective field of view and reduced cost.

Keywords: Monte Carlo simulations; GEANT4; positron emission tomography; scintillation photons; GEANT4 simulations; silicon photomultiplier; scintillators; LYSO(Ce)

Academic Editor: Ivor Fleck

Received: 9 December 2024
Revised: 29 January 2025
Accepted: 1 February 2025
Published: 5 February 2025

Citation: Georgadze, A.S. Feasibility Study of a PET Detector with a Wavelength-Shifting Fiber Readout. *Instruments* **2025**, *9*, 2. https://doi.org/10.3390/instruments9010002

1. Introduction

Positron emission tomography (PET) [1] is a powerful and versatile imaging technique which plays a crucial role in the diagnosis and management of a variety of medical conditions, including tumors (cancer), cardiovascular diseases, and neurological disorders. By providing detailed images of metabolic activity and physiological processes at the cellular level, PET offers insights which other imaging modalities, like CT or MRI, may not provide.

Because conventional whole-body PET scanners are not optimized for imaging small structures, there is a growing research focus on developing organ-specific PET scanners [2–5]. These specialized scanners offer improved performance in terms of enhanced spatial resolution and higher sensitivity. They are particularly beneficial for detailed imaging in neurological diseases [6] (e.g., Alzheimer's or Parkinson's disease), where detecting small brain structures is critical. Additionally, they improve the detection of small-sized breast cancers which might not be visible in whole-body scans and enhance the study of

cardiovascular disease and heart metabolism with greater accuracy. By targeting specific organs, these scanners provide a valuable tool for early diagnosis, monitoring disease progression, and evaluating treatment response, offering higher diagnostic accuracy for specialized clinical applications [7,8]. Alternatively, total-body PET offers an approach to significantly enhance the sensitivity and imaging resolution of positron emission tomography (PET) [9]. Total-body PET scanners cover the entire human body, enabling the detection of a larger proportion of emitted photons and thereby significantly enhancing sensitivity.

PET imaging uses a positron-emitting radioactive tracer, such as ^{18}F, which is injected into the patient's body. Commercial PET scanners typically employ scintillation crystal arrays arranged in a ring around the human body. These arrays detect the two 511 keV γ photons emitted in opposite directions as a result of positron annihilation. This configuration allows for the localization of both annihilation photon interactions, creating a line of response (LOR) which is used for image reconstruction in PET.

For PET scanners, parallax errors become a significant issue when γ rays hit the detector at an angle, leading to inaccuracies in determining the LOR. This angular deviation causes errors in reconstructing the interaction position, which negatively impacts image quality. Therefore, accurate determination of the depth of interaction (DOI) or, more precisely, the 3D reconstruction of the first interaction position, is a primary focus of research in PET technology. For pixelated PET detectors, one of the common methods for acquiring the DOI is the dual-ended readout technique. This method uses photodetectors on both ends of the scintillation crystal to measure the light output, allowing the system to estimate the position of the γ–photon interaction along the depth of the crystal [10,11]. However, a dual-sided readout of scintillators requires a larger number of photosensors, which increases the overall detector costs.

In monolithic crystal-based PET detectors [3,12–16], the DOI can be inferred based on the pattern of scintillation light detected by the photosensors coupled to the crystal [17,18]. In recent years, there has been growing interest in using PET detectors based on monolithic crystals as an alternative to conventional pixelated scintillation crystal arrays. Monolithic crystals offer several advantages in terms of performance and flexibility, particularly in improving spatial resolution, sensitivity, and timing precision, making them a promising choice for next-generation PET systems [13,14,19,20].

In this paper, we explore a new detection technology based on the use of wavelength shifters (WLSs) to read out scintillation light, as opposed to direct photosensor readout. The detector scheme is shown in Figure 1). The detector design includes WLS fibers placed along both long sides of a flat crystal scintillator in orthogonal directions, allowing the x, y, and z coordinates of the interaction point to be reconstructed. This configuration enables accurate three-dimensional position reconstruction, improving the overall performance of the detection system.

Since the size of monolithic scintillators is limited by production technology, multiple crystals are combined into a matrix assembly using optical adhesive coupling, enabling larger detection surfaces without compromising performance. The performance of the optically coupled crystal assembly was studied in [21–23], and the results suggest a reduction in edge effects and improved uniformity of the light pattern across the entire sensitive area. The method for extracting DOI information in PET detectors using wavelength shifting material (WLS) was originally proposed in [24,25], where WLS fibers were orthogonally arranged on the top and bottom of a scintillator array for a signal readout. This approach was also explored in [21–23,26,27].

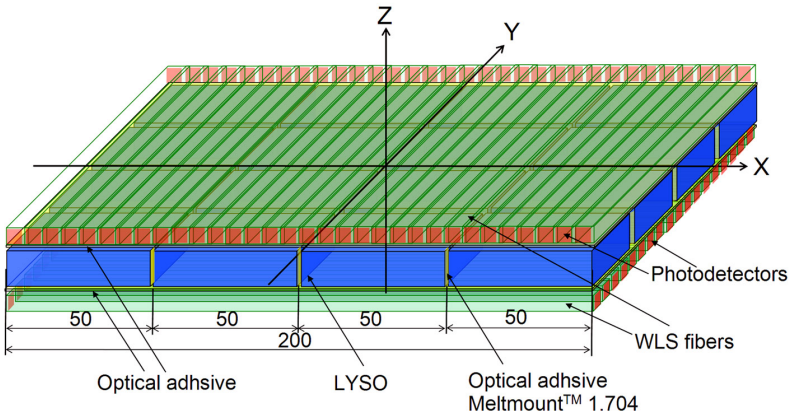

Figure 1. Schematic of detector module composed of a 4 × 4 assembly of LYSO crystals. Red boxes represent SiPMS, blue cubes represent the individual LYSO scintillators, and green rectangles represent the WLS fibers.

2. Detector Design

The PET detector, utilizing a WLS-fiber readout (WLS-PET), is composed of a 4 × 4 assembly of monolithic LYSO crystal scintillators arranged in a planar geometry with dimensions of 50 × 50 × 15 mm^3. The crystals are optically coupled together using an optical adhesive (Meltmount^{TM} with a refractive index of 1.704 [28]) to create a detector with a large sensitive area. The 3 × 3 mm^2 WLS square-shaped, wavelength-shifting (WLS) fibers (BCF-91A) are placed in orthogonal directions (X and Y) on each side of the crystal assembly. This arrangement allows for the reconstruction of hit position information. To improve light collection efficiency, the WLS fibers are optically coupled to the crystals. The outer detector layer, which covers the WLS fibers on the top and bottom, is made of 3M^{TM} Enhanced Specular Reflector (ESR) film [29], which enhances the efficiency of light collection by reflecting any scattered light back into the WLS fibers. WLS fibers are read out at both ends using silicon photomultipliers (SiPMs). To prevent reflections from the lateral faces of the crystals, the crystals were painted black. The schematic of the detector is shown in Figure 1. The number of WLS fibers on each side of the 4 × 4 crystal array is 66. The WLS-fiber pitch is 3.03 mm, which refers to the distance between the centers of adjacent wavelength-shifting fibers in the detector array. This pitch determines the granularity of light distribution binning and directly affects the position resolution achievable in the system.

3. Monte Carlo Simulation of the Detector

In the GEANT4 [30] simulation (version Geant4-10.7.4) for this study, all relevant physical processes were included to ensure accurate modeling of photon interactions within the PET detector. The following electromagnetic processes, such as ionization, bremsstrahlung, multiple scattering, pair production, Compton scattering, and the photoelectric effect, were considered. The optical processes included scintillation, Cherenkov radiation, volume absorption, Rayleigh scattering, and boundary processes like reflection, refraction, and absorption. The Birks effect, which adjusts the scintillation light yield to account for variations in the energy deposition density by ionizing particles, was accounted for. For optical photon transport, the GLISUR model [31,32] in the GEANT4 package was employed. This model simulates the interactions of optical photons at the interfaces between different materials by applying the concept of optical surfaces to describe light reflection and transmission at the boundaries between media, accounting for scattering, absorption, and reflection. In the GEANT4 detector model, we define the surface roughness for all interfaces. When the polish parameter is set to zero, this represents the maximum roughness, where photons

are reflected according to a Lambertian distribution. Conversely, a polish value of one applies Snell's law. All material optical interface types were modeled as dielectric-dielectric, with the exception of the ESR foil-to-air and SiPM window-to-SiPM material interfaces, which were modeled as dielectric-metal. The reflectance for the ESR foil was set to 0.98 in the spectral range of visible light. For the simulations, all surfaces were considered to be ground with polish values ranging from 0.8 to 0.95.

The selection of lutetium yttrium orthosilicate (LYSO) as the scintillator material for the proposed WLS-PET detector was based on its excellent properties, which make it well suited for high-performance positron emission tomography (PET) applications. LYSO has a high light yield, a fast decay time, and a high effective atomic number (Z_{eff}), making it an ideal candidate for efficient gamma ray detection. Its short radiation length allows for compact detector designs, and its non-hygroscopic nature ensures long-term stability compared with other scintillator materials like NaI or $LaBr_3$, which are more prone to moisture absorption. Additionally, as shown in Figure 2, LYSO has a peak emission wavelength of about 420 nm, which matches well with the absorption spectra of the BCF-91A WLS fibers used in the detector design, enabling efficient light transport and signal detection. None of the other crystal scintillators listed in the table provide such a strong match. Other materials, such as $CdWO_4$, exhibit shorter radiation lengths but have longer decay times of 14,000 ns, making them unsuitable for PET applications, where the timing resolution is crucial. Table 1 shows the values of the properties for several common scintillator materials [33].

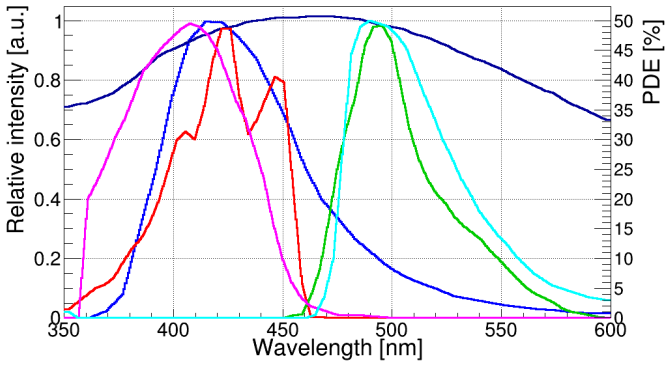

Figure 2. Photon emission spectrum of LYSO scintillator [34] (blue color), absorption (red color), and emission (green color) spectra of BCF-91A [35], SiPM PDE (dark blue color), and absorption (magenta color) and emission (dark green color) spectra of BCF-92 [35].

Table 1. Basic properties of common scintillation crystals.

Material	Density (g/cm^3)	Emission Maximum (nm)	Decay Constant (ns)	Refractive Index	Light Yield (ph/keV)	Radiation Length (cm)
Na(Tl)	3.67	415	250	1.83	41	2.59
CaF_2	3.18	435	950	1.47	20	3.5
YAG(Ce)	4.6	500–700	70	1.82	8	3.5
CsI(Tl)	4.51	550	1000	1.79	52	1.86
GSO(Ce)	6.71	440	30–60	1.85	8–10	1.38
GLuGAG	6.8	450–650	75	1.81	50	1.26
LYSO(Ce)	7.4	420	40	1.82	32	1.15
BGO	7.13	480	300	2.15	8.5	1.13
$CdWO_4$	7.9	470/540	14,000	2.3	13	1.06

LYSO's effective atomic number of 66 and density of 7.4 g/cm^3 provide a short attenuation length of 11.5 mm for 511 keV γ rays, corresponding to an interaction probability of

approximately 73 % within a 15 mm thick crystal. The LYSO scintillator light yield ranges from 26,000/MeV to 39,900/MeV [34,36–40]. In the simulation, the light yield of LYSO was set to 26,000 photons/MeV, the scintillation decay time was set to 43 ns, and the light attenuation length was set to 40 cm [40].

The WLS fiber used in the simulations was the square-shaped double-clad BCF-91A [35], which had an absorption peak at 420 nm and an emission peak at 494 nm. The polystyrene core of the BCF-91A WLS fiber had a refractive index of 1.6, while the refractive index of the first cladding layer (acrylic) was 1.49, and the second cladding layer (fluor-acrylic) had a refractive index of 1.42.

WLS fibers were coupled to the LYSO assembly using Meltmount optical adhesive (refractive index n = 1.58), which was also used to connect the WLS fibers to the SiPMs. The use of optical glue significantly enhanced the number of optical photons transmitted from the crystal to the fibers. This improvement was due to the fact that the critical angle at the LYSO-optical glue interface was greater than that at the LYSO-air interface, allowing considerably more photons to pass through the interface. As a result, this coupling method improved the overall light collection efficiency and enhanced the performance of the WLS-PET detector.

The SiPM was modeled as a material made of silicon (Si) with a window size of 3×3 mm^2. The Hamamatsu S13360 CS75 series SiPM was used as the benchmark unit for this study. The light detection efficiency was calculated by weighting the SiPM's photon detection efficiency (PDE) with the emission spectra of the BCF-91A WLS fiber, yielding a value of approximately 40%. Simulations were also conducted with an LYSO array readout using BCF-92 WLS fiber, which served as an alternative to BCF-91A WLS. As shown in Figure 2, the absorption spectrum of the BCF-92 fiber did not matched as well with the emission spectrum of LYSO. However, its short decay time of 3 ns makes it a viable option when the long decay time ($\tau > 10$ ns) of the BCF-91A fiber significantly affects the annihilation gamma coincidence detection efficiency in PET applications.

The developed simulation model and the optical properties of the materials were validated against experimental data on the light response of the LYSO scintillator. A GEANT4 model, described in [34], was created, and the parameters were adjusted until agreement was achieved with the energy resolution data presented in the publication. The simulation parameters for the WLS fibers were further adjusted in accordance with [41] to accurately represent the light collection and transmission properties.

4. Results

The GEANT4 application was run to generate data samples which recorded the number of optical photons detected by each SiPM. The simulated data were recorded event by event in CERN ROOT [42] in TTree format and then analyzed using a C++ code. In the simulation, a pencil beam of 511 keV photons was incident perpendicularly onto the LYSO scintillator block at various positions across the detector surface. A total of 20,000 events were simulated for each beam position to accurately represent the photon interactions within the scintillator material.

Optical photons generated by annihilation gammas travel through the optically coupled LYSO scintillators and reach the black-painted lateral surfaces of the crystal assembly, where they are absorbed. Some of these photons are directed toward the WLS fibers, where they are absorbed and re-emitted at longer wavelengths, allowing them to be directed toward the SiPMs for detection. This process enables efficient light collection and position reconstruction for precise tracking of the annihilation gamma interactions. Figure 3 illustrates an example of the tracking of optical photons within the WLS-PET detector.

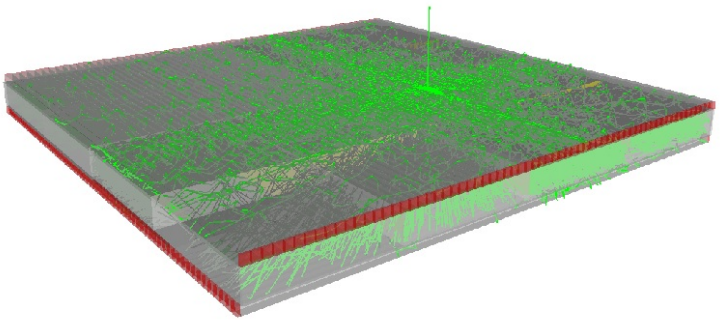

Figure 3. Example of one event with the secondary scintillation photons simulated in GEANT4 for a LYSO assembly. The light green lines are the tracks of optical photons, and the red boxes are SiPMs.

There are several event positioning algorithms in PET detectors, such as weighted energy centroid positioning (Anger logic) [43], a machine learning-based positioning algorithm [44,45], or statistical methods, such as least squares, nearest neighbors, and the maximum likelihood [2]. In this work, the (x, y, z) positions are reconstructed using an in-house developed algorithm, which analyzes the light distribution patterns within the detector using the ROOT peak search function.

The simulated data represent the distribution of the number of photons detected by the SiPMs connected to both the upper (x axis) and lower (y axis) WLS fibers. The examples of such distributions are shown in Figures 4 and 5 (more figures can be found in [46]).

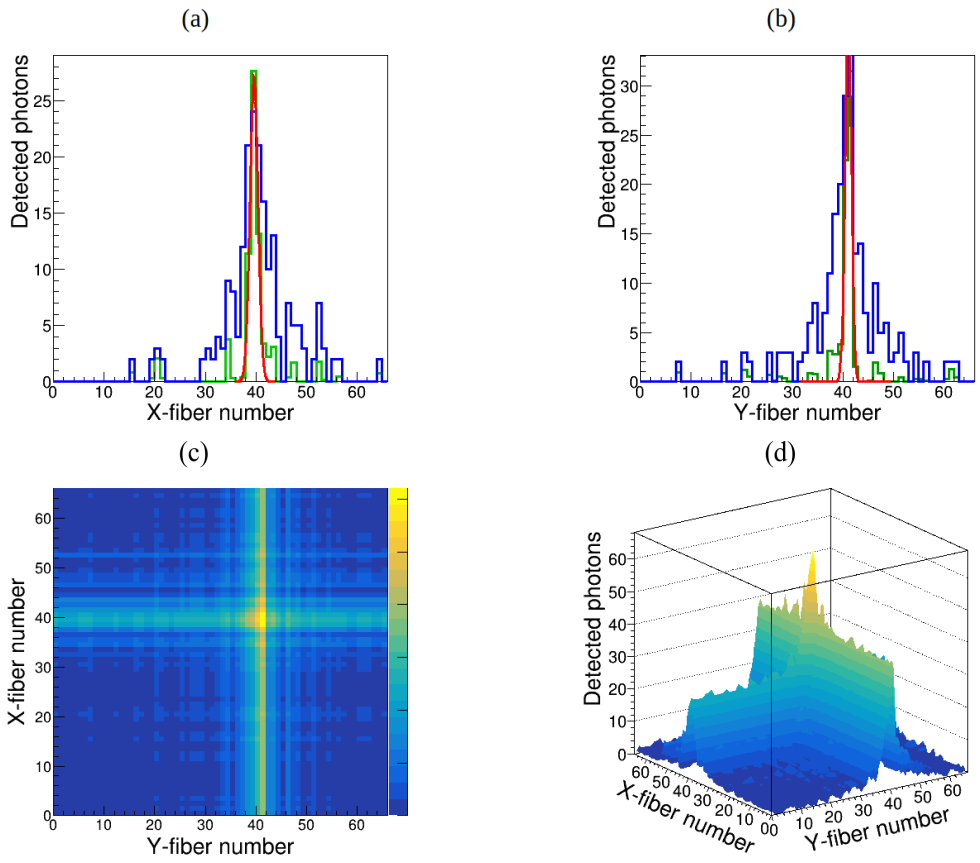

Figure 4. (**a**,**b**) The light distribution profiles along the x (**a**) and y (**b**) directions in a typical event displaying photoelectron absorption-like behavior. The simulated data were fitted with a Gaussian function. The blue histogram is the simulated results, and the red histogram is the Gaussian fitting, while the green histogram is a high-resolution peak search function. (**c**) The x–y distribution image obtained by combining signals from the x and y WLS fibers. (**d**) The x–y distribution image in 3D.

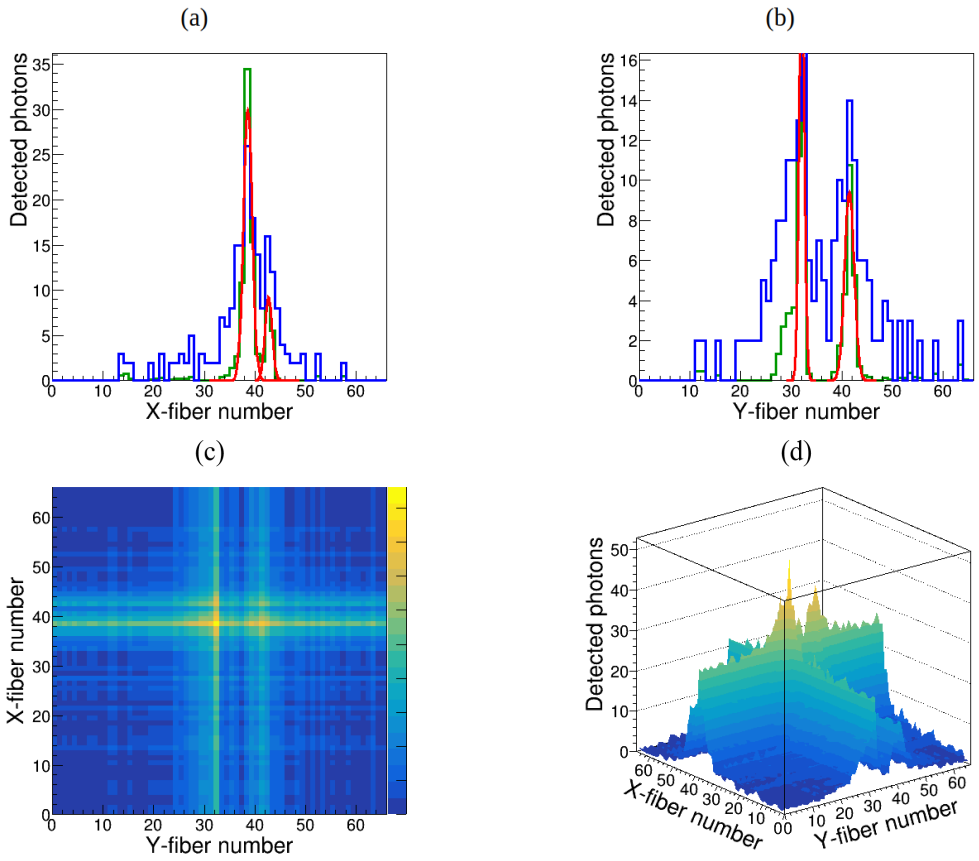

Figure 5. (**a**,**b**) The light distribution profiles along the x (**a**) and y (**b**) directions in a typical event displaying the Compton scattering event event. The simulated data were fitted with a Gaussian function. The blue histogram is the simulated results, and the red histogram is the Gaussian fitting, while the green histogram is a high-resolution peak search function. (**c**) The x–y distribution image obtained by combining signals from the x and y WLS fibers. (**d**) The x–y distribution image in 3D.

The γ ray hit position was calculated for the x and y axes. For each simulated event, the distributions of detected photons were analyzed using a high-resolution peak searching function (class TSpectrum) in the ROOT package. The identified peaks were further fitted with Gaussian functions, with the mean values corresponding to the x and y coordinates of the interaction position. If a single peak was detected, then the event was identified as photoelectric absorption. In contrast, if multiple peaks were detected, then the event was classified as Compton scattering and could be excluded from further analysis, as it typically resulted in a complicated light distribution requiring the application of Compton kinematic reconstruction methods. An example of such an event with two peaks detected in the light distribution is illustrated in Figure 5.

In photoelectric absorption events, a single isotropic source of scintillation light is produced precisely at the location where the 511 keV photon is absorbed. The emitted light propagates uniformly in all directions from this point, enabling straightforward determination of the interaction position based on the resulting light distribution pattern. In contrast, Compton scattering generates two or more scintillation points within the crystal, leading to a more complex light distribution. This added complexity makes it challenging to accurately pinpoint the primary interaction position.

In this study, as a feasibility approach, we limited the analysis to classifying events and rejecting those identified as Compton scattering. However, in future work, we plan to extend the methodology by incorporating Compton kinematic reconstruction, enabling the inclusion of Compton scattering events in the analysis to further enhance the system's capabilities.

Figure 6 shows the reconstructed interaction positions of a 511 keV γ ray beam modeled at positions (x, y) = (20 mm, 15 mm) for crystal thicknesses of 7 mm (a,b) and 15 mm (c,d). The spatial resolution was calculated for each point source position as the FWHM and FWTM of the light spread function (LSF) determined in two dimensions. As can be seen in these figures, the FWTM values increased more significantly with an increasing crystal thickness compared with the FWHM. This is because with thicker crystals, there is a higher probability of detecting Compton-scattered gamma rays at locations further away from the first interaction position. Such events may be incorrectly reconstructed as the first interaction position, resulting in a wider FWTM value. To localize the interaction position, the distributions of detected photons in the x and y WLS fibers were fitted with Lorentzian functions. The mean value of the Lorentzian functions corresponded to the x and y coordinates of the 511 keV γ ray interaction position. The resulting distribution shows that the Compton scatterings did not have a strong effect on the width of the peak but created a noise-like plateau.

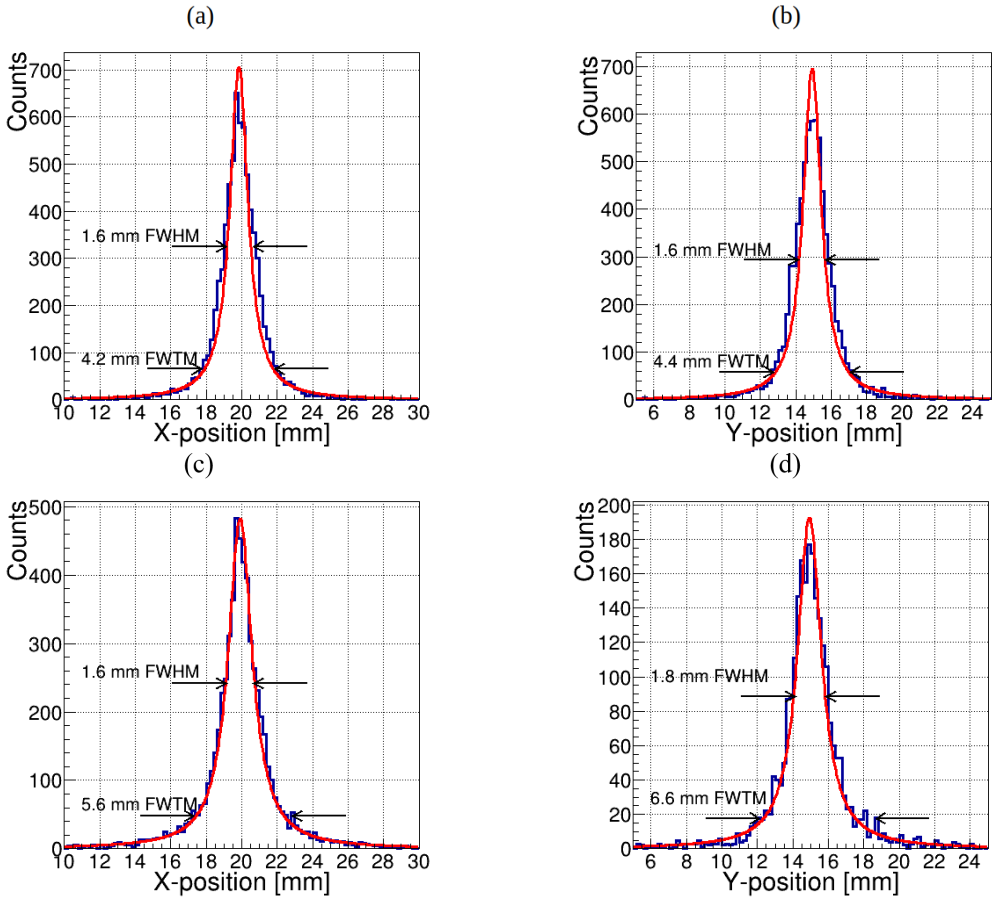

Figure 6. Histogram of reconstructed interaction positions (blue line) of a 511 keV γ ray beam positioned at (x, y) = (20 mm, 15 mm) for a crystal thickness of 7 mm (**a**,**b**) and for a crystal thickness of 15 mm (**c**,**d**). A Lorentzian fit to the distribution is also shown (red line).

The reconstructions of two hit positions in the XY plane are shown in Figure 7 for a crystal thickness of 7 mm and in Figure 8 for a crystal thickness of 15 mm, corresponding to beam positions at (x, y) = (15 mm, 15 mm) and (x, y) = (20 mm, 15 mm). It can be observed that position discrimination was significantly better for the 7 mm thick crystal compared with the 15 mm thick crystal. This is attributed to the fact that in thicker crystals, a Compton-scattered γ photon can travel a considerable distance from the initial interaction point, resulting in a broader light spread function (LSF).

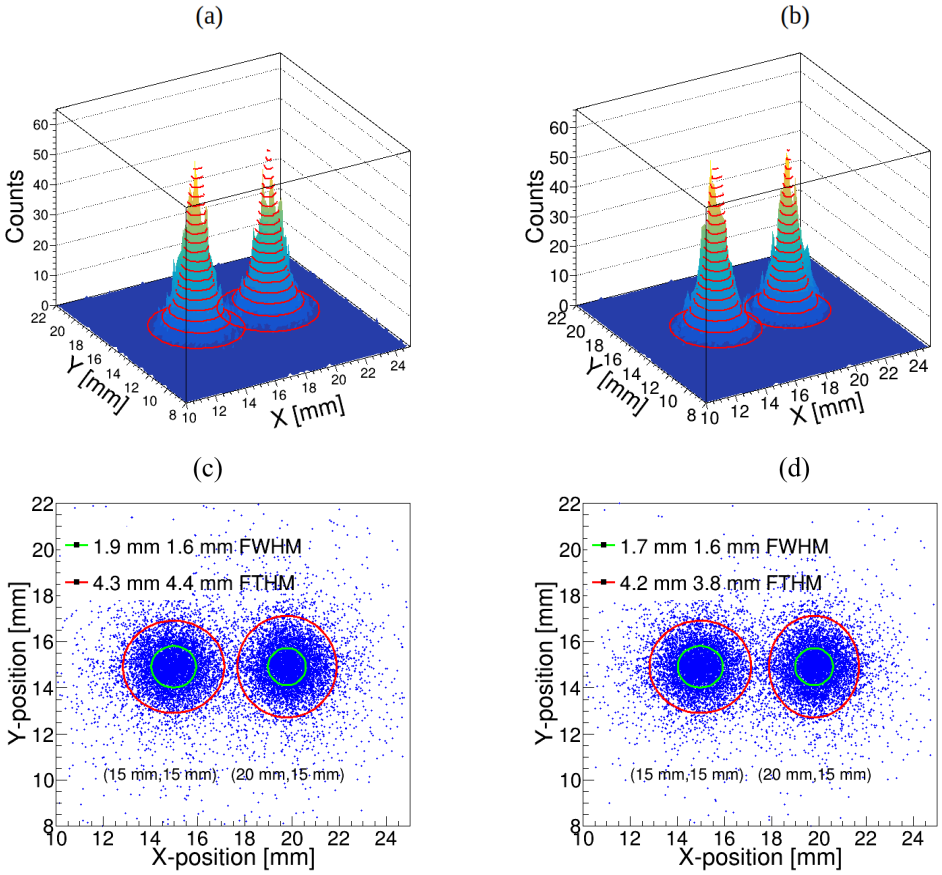

Figure 7. XY histograms of interaction position reconstruction of the 511 keV γ ray beams positioned at (x, y) = (15 mm, 15 mm) and (x, y) = (20 mm, 15 mm), shown in both 3D (top) and 2D (bottom) representations (blue dots) for a crystal thickness of 7 mm: (**a**,**c**) no rejection and (**b**,**d**) with Compton scattering events rejection applied.

The timing resolution of the proposed detector design was studied by simulating the time spectra of the scintillation photons detected by the SiPMs. The timing resolution is a critical characteristic as it enables high detection efficiency for coincidence events within a specified time window. The simulated response time spectra of detected photons in a single event for 511 keV energy deposition in a LYSO crystal array read out using BCF-91A and BCF-92 WLS fibers are shown in Figure 9a,b, respectively. The modeled response time of the WLS-based LYSO crystal assembly readout was comparable to that of a detector composed of a 13 × 13 LYSO crystal array coupled to a 6 × 6 SiPM array [47]. However, it was observed that the BCF-91A fiber exhibited a relatively slow decay time (τ_d > 10 ns), which resulted in an increased signal duration compared with the BCF-92 WLS fibers. The BCF-92 fibers had a shorter decay time, but their sensitivity was lower due to the poorer matching between their absorption spectra and the luminescence spectrum of the LYSO crystal. The averaged time response over 2000 events to 511 keV γ ray irradiation of the WLS-PET detector (with a 15 mm thick LYSO crystal) readout with BCF-91A and BCF-92 fibers is shown in Figure 9c. The scintillation decay time remained the same for the WLS-PET detector with both BCF-91A and BCF-92 fibers.

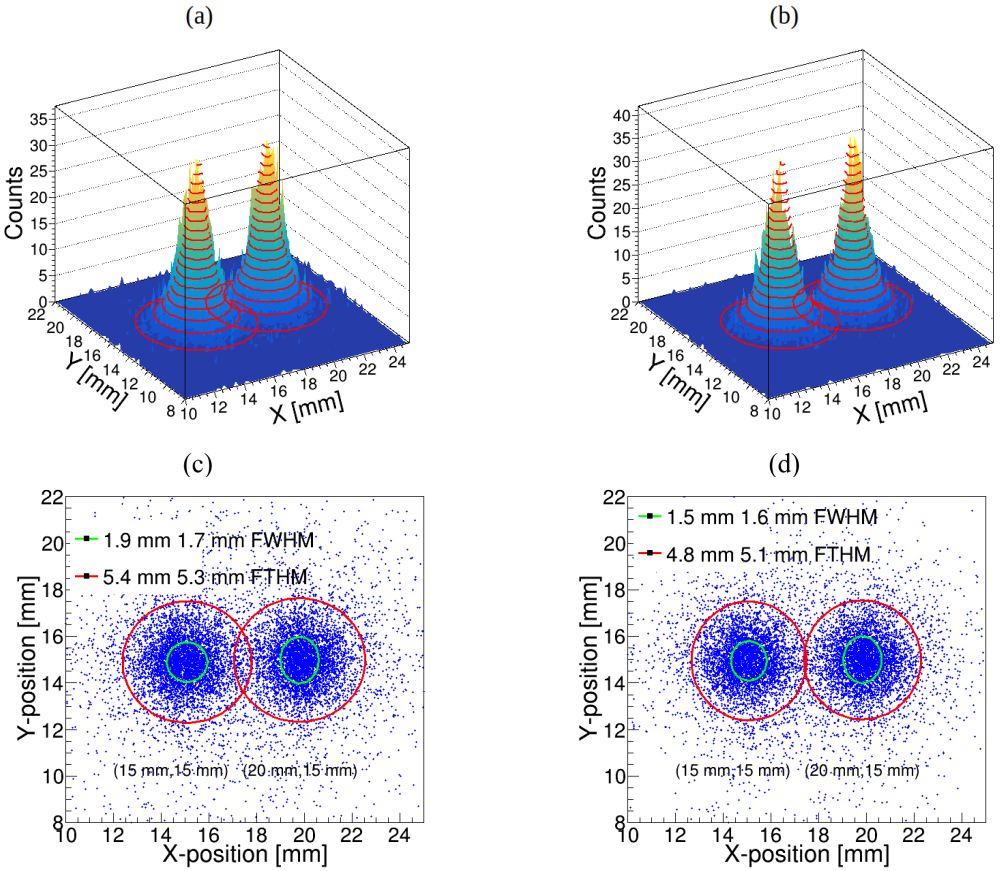

Figure 8. XY histograms of interaction position reconstruction of the 511 keV γ ray beams positioned at (x, y) = (15 mm, 15 mm) and (x, y) = (20 mm, 15 mm), shown in both 3D (top) and 2D (bottom) representations (blue dots) for a crystal thickness of 15 mm: (**a**,**c**) no rejection and (**b**,**d**) with Compton scattering events rejection applied.

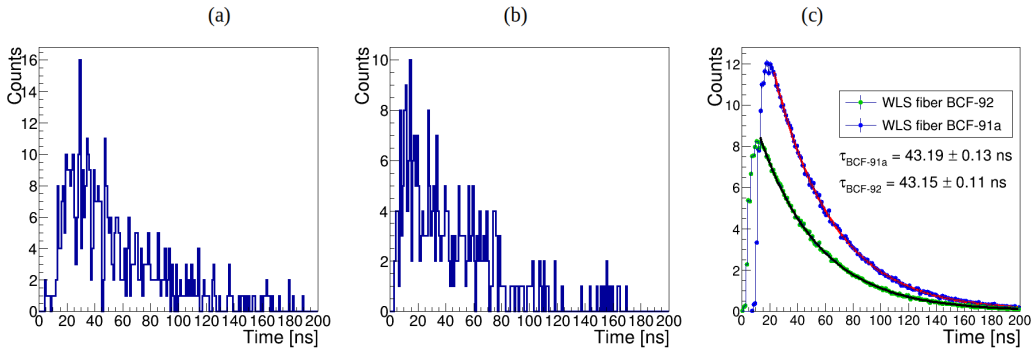

Figure 9. Response time spectrum of detected photons in a single event for 511 keV energy deposition in a LYSO crystal array readout using BCF-91A fibers (**a**) and BCF-92 fibers (**b**). (**c**) The average (n = 2000) response time spectrum of detected photons for 511 keV energy deposition in a LYSO crystal array, shown for the readout with BCF-91A fibers (blue histogram fitted with an exponential function in red) and the readout with BCF-92 fibers (green histogram fitted with an exponential function in black).

In monolithic crystal-based detector designs, a key challenge is the truncation of scintillation light at the edges, which negatively impacts the spatial, timing, and energy resolutions in these regions. Various methods have been tested to mitigate this effect, including crystal surface treatments, such as covering the edges with an optical absorber, and innovative photodetector arrangements. In the proposed detector geometry, 16 crystals are coupled together, forming a semi-monolithic large area detector. Uniform detection of

annihilation gammas across the detector area was assessed through simulations of 511 keV γ rays impinging perpendicularly on the detector surface at a 20 $\times$ 20 grid of points spaced 10 mm apart. As shown in Figure 10a, the combination of the applied ROOT-based positioning algorithm and the developed detector design achieved a uniform system spatial resolution across the entire field of view.

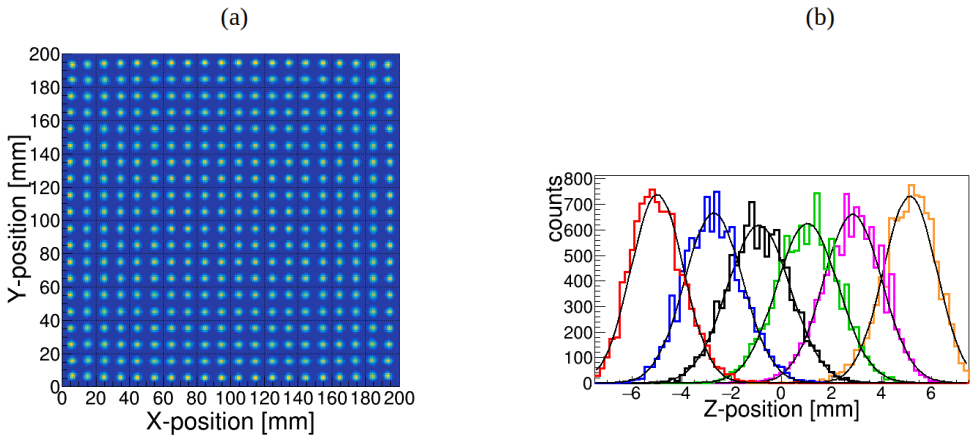

Figure 10. (**a**) A 2D histogram of the positioning estimations using a ROOT-based algorithm, demonstrating interaction uniformly distributed across a grid of 20 $\times$ 20 points spaced 10 mm apart. (**b**) The z-coordinate of the interaction position, simulated at six depths, regarded as the depth-of-interaction (DOI) resolution.

The (x,y,z) coordinates were reconstructed in three dimensions: two planar coordinates (x,y) in combination with the coordinate (z) within the crystal. The light asymmetry was used for the determination of the axial coordinate z:

$$z = \frac{L}{2} \cdot \frac{N_{upper} - N_{lower}}{N_{upper} + N_{lower}}, \quad (1)$$

where N_{upper} and N_{lower} are the number of optical photons detected by SiPMs in the upper and lower WLS fibers, respectively, in a crystal assembly with a thickness L. The reconstructed z coordinate of the interaction position is shown in Figure 10b. The obtained resolution in the z direction was approximately 3–4 mm FWHM. The distribution of 3D coordinates is shown in Figure 11a,b without rejection of the Compton events and with such a rejection, respectively.

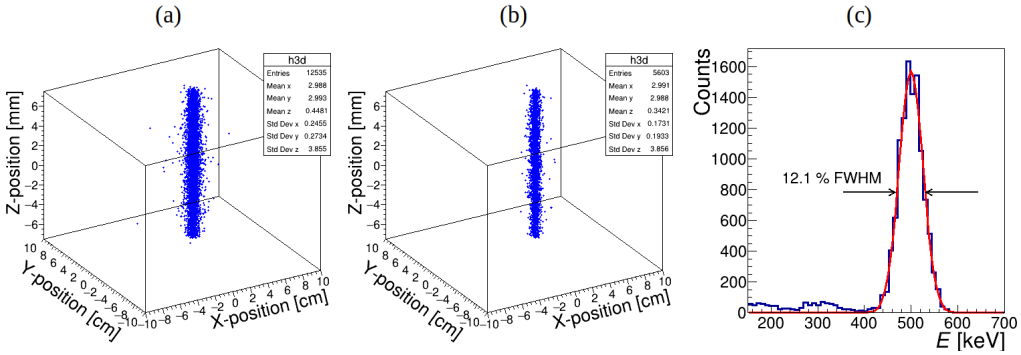

Figure 11. Three dimensional plot of reconstructed (x, y, z) coordinates for the 511 keV γ-ray beam positioned at (x, y) = (30 mm, 30 mm) shown in with no rejection (**a**) and with Compton scattering event rejection applied (**b**). An energy spectrum of 511 keV γ-rays for the modeled WLS-PET detector is shown together with the corresponding Gaussian fit through the corresponding full energy peak (red line) (**c**).

The number of photons detected within the energy window of 400–600 keV was used to determine the energy resolution of the detector. The energy resolution (R_E) of the detector is defined as follows:

$$R_E = \frac{\sigma \times 2.355}{mean} \times 100\%, \quad (2)$$

where σ and *mean* are obtained from the Gaussian fitting of the modeled photoelectron distribution. With the simulation, the obtained an energy resolution was ≈12% (FWHM) (Figure 11c).

The uniformity of the detector sensitivity over the entire detector area was evaluated by examining the variation in the number of detected photons with the position. Figure 12a,b illustrates the local variations in the number of detected photons, which influenced the variation in energy calibration and energy resolution across the detector surface.

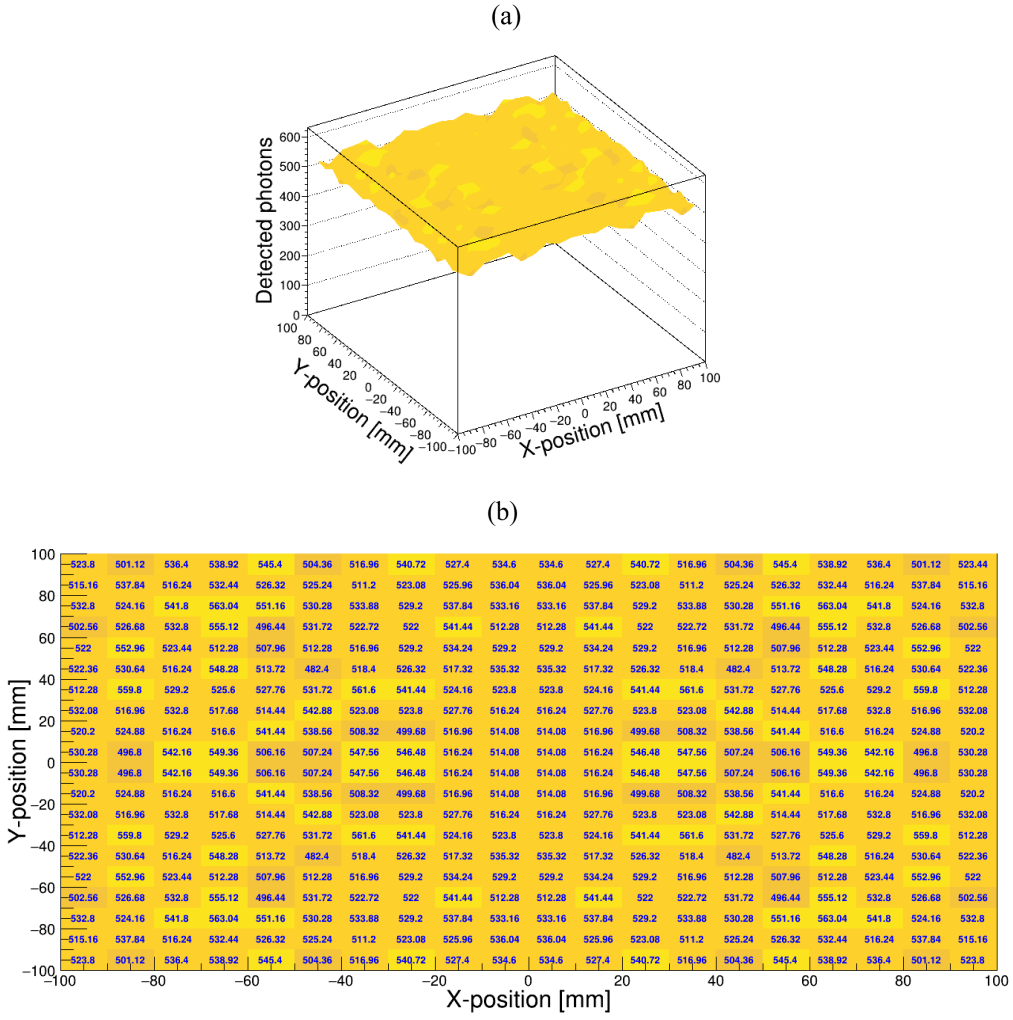

Figure 12. The 3D (**a**) and 2D (**b**) histograms of the average number of detected photons, demonstrating uniformity of energy resolution across the detector's sensitive area. In the histogram, darker yellow bins indicate fewer detected photons, while brighter yellow bins represent a higher number of detected photons.

5. Discussion

In commercial PET systems, the detector typically uses a crystal array which forms a matrix of pixel elements [48]. The scintillation light produced in each pixel element is used to identify the interaction location based on the pixel's position, meaning that the reconstructed interaction positions are limited to discrete values corresponding to the pixel

layout. In contrast, monolithic scintillator detectors capture a continuous light distribution across their surface, which is detected by SiPM pixels, the size of which determines the detection grid. Each pixel covers a specific region of the scintillation crystal, converting the scintillation light into electrical signals. The signal level is proportional to the amount of light hitting the surface of the photodetector pixel, resulting in the continuous light distribution being digitized and organized into bins. Each bin represents a defined region of the scintillation crystal. A smaller bin size allows for more accurate digitization of the light distribution, capturing finer details of the scintillation light pattern. For commercial applications of monolithic-based PET detectors, the size of the SiPMs and the number of detection channels must be optimized to achieve a cost-effective solution while maintaining high performance. The 6×6 mm^2 SiPM arrays are considered an optimal solution to cover large detection areas [49,50].

For the proposed WLS-PET detector design, the WLS-fiber size of 3×3 mm^2 created a detection grid with 66 fibers on each side of the crystal assembly, totaling 132 fibers. This configuration resulted in a "pixel" size of $\approx 3 \times 3$ mm^2. The light was detected by 264 SiPMs, each with an active area of 3×3 mm^2, and the total detector surface area was 2376 mm^2. For comparison, a 16 crystal assembly of LYSO with a surface area of 50 mm $\times$ 50 mm would create a total detector area of 200 mm $\times$ 200 mm, equivalent to the proposed WLS-PET detector design. However, this configuration would require 1089 SiPMs 6×6 mm^2 in size, with a total area of 39,204 mm^2.

This resulted in the total SiPM area for the WLS-PET design being just 6% of that required for a traditional SiPM-based design. Despite the smaller photosensor area, the WLS-PET detector design supports the creation of a much finer detection grid, enabling detailed reconstruction of gamma ray interactions within the crystal. This fine granularity facilitates the application of multiple Gaussian fittings to the light distribution, which was used in the partial rejection of Compton scattering events, thereby enhancing the spatial resolution.

Coincidence timing resolution (CTR) is a critical performance parameter for PET systems [51]. Estimating the CTR requires the development of a full-ring PET geometry study, which is not feasible with the current WLS-PET detector model. Therefore, the CTR was not evaluated in this work. However, since the timing characteristics of the proposed WLS-PET detector are similar to those of monolithic scintillator-based PET systems [52], we expect that the CTR of WLS-PET will be comparable to that of monolithic scintillator PET systems.

As shown in this work, the FWTM values increased more significantly with the crystal thickness compared with the FWHM, resulting in a deterioration in the position resolution. Although thinner crystals improved the spatial resolution, this improvement came at the expense of decreased detection efficiency. To address this issue, the advantage of the proposed design, the reduced number of photodetectors, can be used to optimize the detector configuration. Implementing a detector geometry with two thin layers, each 7 mm thick, will maintain high gamma ray detection efficiency and excellent spatial resolution while still using significantly fewer photodetectors compared with a direct crystal readout with SiPM. Moreover, this approach will transform the detector into a Compton camera, enabling more effective localization of the annihilation gamma source.

The proposed novel WLS-PET detector design can be used in the construction of organ-specific or whole-body PET scanners, as the drastic reduction in the number of SiPMs and readout channels makes the design cost-effective while maintaining an extremely high spatial resolution. Figure 13 illustrates the schematic designs of potential PET scanner configurations: (a) an organ-specific scanner and (b) a total-body PET scanner.

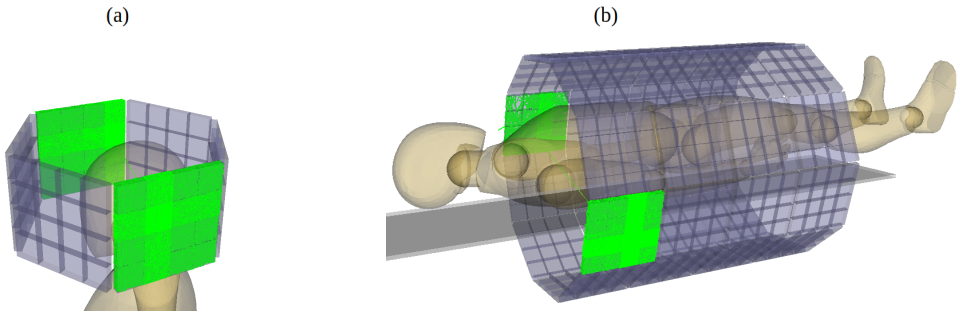

Figure 13. Schematic of a brain PET scanner (**a**) and a total-body PET scanner (**b**), both composed of modules from a 4 × 4 assembly of optically coupled LYSO crystals (gray). The interaction of annihilation γ-rays with the opposite detection modules produces scintillation photons (green), which are shared within the LYSO assembly due to optical coupling. WLS fibers are not shown.

6. Conclusions

In this work, the performance of the designed WLS-PET detector featuring an assembly of optically coupled monolithic crystals with large surface areas of 200 × 200 mm^2 and LYSO crystal thicknesses of 7 mm and 15 mm was evaluated. The detector utilizes 3 mm WLS fibers with square cross-sections for light readouts, providing a fine detection grid while maintaining a simplified and cost-effective design. This configuration enables a high spatial resolution and efficient gamma ray interaction localization, demonstrating its potential for advanced PET imaging applications. In the proposed WLS-PET detector, the interaction position of annihilation γ rays within the scintillation crystal assembly is determined by measuring the light profiles trapped in wavelength-shifting (WLS) fibers coupled to the crystal assembly. The detector achieved a position resolution of approximately 1.6 ± 0.4 mm FWHM and 4.2 ± 0.6 mm FWTM for the 7 mm LYSO crystal thickness and 1.7 ± 0.4 mm FWHM and 6.0 ± 0.6 mm FWTM for the 15 mm LYSO crystal thickness.

A spatial resolution compatible with commercial detectors was achieved while significantly reducing the number of SiPMs and readout channels required.

Funding: This research received no external funding.

Data Availability Statement: Figures illustrating the distribution of detected photons with the WLS-PET detector are available in the Mendeley Data Repository: https://doi.org/10.17632/g4zfp9g3nh.1.

Conflicts of Interest: The author declares no conflicts of interest.

References

1. Gonzalez-Montoro, A.; Ullah, M.N.; Levin, C.S. Advances in detector instrumentation for PET. *J. Nucl. Med.* **2022**, *63*, 1138–1144. [CrossRef]
2. Gonzalez-Montoro, A.; Gonzalez, A.J.; Pourashraf, S.; Miyaoka, R.S.; Bruyndonckx, P.; Chinn, G.; Pierce, L.A.; Levin, C.S. Evolution of PET detectors and event positioning algorithms using monolithic scintillation crystals. *IEEE Trans. Radiat. Plasma Med. Sci.* **2021**, *5*, 282–305. [CrossRef]
3. Moliner, L.; Gonzalez, A.; Soriano, A.; Sanchez, F.; Correcher, C.; Orero, A.; Carles, M.; Vidal, L.; Barbera, J.; Caballero, L.; et al. Design and evaluation of the MAMMI dedicated breast PET. *Med. Phys.* **2012**, *39*, 5393–5404. [CrossRef] [PubMed]
4. Jones, T.; Rabiner, E.A. The development, past achievements, and future directions of brain PET. *J. Cereb. Blood Flow Metab.* **2012**, *32*, 1426–1454. [CrossRef] [PubMed]
5. Catana, C. Development of dedicated brain PET imaging devices: Recent advances and future perspectives. *J. Nucl. Med.* **2019**, *60*, 1044–1052. [CrossRef]
6. Xie, L.; Zhao, J.; Li, Y.; Bai, J. PET brain imaging in neurological disorders. *Phys. Life Rev.* **2024**, *49*, 100–111. [CrossRef]
7. Taha, A.; Alassi, A.; Gjedde, A.; Wong, D.F. Transforming Neurology and Psychiatry: Organ-specific PET Instrumentation and Clinical Applications. *PET Clin.* **2024**, *19*, 95–103. [CrossRef]
8. Stiles, J.; Baldassi, B.; Bubon, O.; Poladyan, H.; Freitas, V.; Scaranelo, A.; Mulligan, A.M.; Waterston, M.; Reznik, A. Evaluation of a high-sensitivity organ-targeted PET camera. *Sensors* **2022**, *22*, 4678. [CrossRef]

9. Katal, S.; Eibschutz, L.S.; Saboury, B.; Gholamrezanezhad, A.; Alavi, A. Advantages and Applications of Total-Body PET Scanning. *Diagnostics* **2022**, *12*, 426. [CrossRef]
10. Stickel, J.R.; Cherry, S.R. High-resolution PET detector design: Modelling components of intrinsic spatial resolution. *Phys. Med. Biol.* **2004**, *50*, 179. [CrossRef]
11. Yang, Y.; Wu, Y.; Qi, J.; James, S.S.; Du, H.; Dokhale, P.A.; Shah, K.S.; Farrell, R.; Cherry, S.R. A prototype PET scanner with DOI-encoding detectors. *J. Nucl. Med.* **2008**, *49*, 1132–1140. [CrossRef] [PubMed]
12. Schaart, D.R.; van Dam, H.T.; Seifert, S.; Vinke, R.; Dendooven, P.; Löhner, H.; Beekman, F.J. A novel, SiPM-array-based, monolithic scintillator detector for PET. *Phys. Med. Biol.* **2009**, *54*, 3501. [CrossRef] [PubMed]
13. Yoshida, E.; Inadama, N.; Osada, H.; Kawai, H.; Nishikido, F.; Murayama, H.; Tsuda, T.; Yamaya, T. Basic performance of a large area PET detector with a monolithic scintillator. *Radiol. Phys. Technol.* **2011**, *4*, 134–139. [CrossRef] [PubMed]
14. González, A.J.; Aguilar, A.; Conde, P.; Hernández, L.; Moliner, L.; Vidal, L.F.; Sánchez, F.; Sánchez, S.; Correcher, C.; Molinos, C.; et al. A PET design based on SiPM and monolithic LYSO crystals: Performance evaluation. *IEEE Trans. Nucl. Sci.* **2016**, *63*, 2471–2477. [CrossRef]
15. Sánchez, F.; Orero, A.; Soriano, A.; Correcher, C.; Conde, P.; González, A.; Hernández, L.; Moliner, L.; Rodríguez-Alvarez, M.J.; Vidal, L.; et al. ALBIRA: A small animal PET/SPECT/CT imaging system. *Med. Phys.* **2013**, *40*, 051906. [CrossRef]
16. Mollet, P.; Deprez, K.; Vandeghinste, B.; Neyt, S.; Marcinkowski, R.; Vandenberghe, S.; Van Holen, R. The β-CUBE, a high-end compact preclinical benchtop PET for total body imaging. *J. Nucl. Med.* **2017**, *58*, 393.
17. Morrocchi, M.; Ambrosi, G.; Bisogni, M.G.; Bosi, F.; Boretto, M.; Cerello, P.; Ionica, M.; Liu, B.; Pennazio, F.; Piliero, M.A.; et al. Depth of interaction determination in monolithic scintillator with double side SiPM readout. *EJNMMI Phys.* **2017**, *4*, 11. [CrossRef]
18. Díaz-Martínez, V.D.; Ambrosio-Macías, N.I.; Murrieta-Rodríguez, T.; Martínez-Dávalos, A.; Rodríguez-Villafuerte, M.; Alva-Sánchez, H. Depth of interaction in monolithic scintillators for positron emission tomography. *Proc. AIP Conf. Proc.* **2021**, *2348*, 050004.
19. Cabello, J.; Barrillon, P.; Barrio, J.; Bisogni, M.G.; Del Guerra, A.; Lacasta, C.; Rafecas, M.; Saikouk, H.; Solaz, C.; Solevi, P.; et al. High resolution detectors based on continuous crystals and SiPMs for small animal PET. *Nucl. Instrum. Methods Phys. Res. Sect. A Accel. Spectrometers Detect. Assoc. Equip.* **2013**, *718*, 148–150. [CrossRef]
20. España, S.; Marcinkowski, R.; Keereman, V.; Vandenberghe, S.; Van Holen, R. DigiPET: Sub-millimeter spatial resolution small-animal PET imaging using thin monolithic scintillators. *Phys. Med. Biol.* **2014**, *59*, 3405. [CrossRef]
21. Freire, M.; Echegoyen, S.; Gonzalez-Montoro, A.; Sanchez, F.; Gonzalez, A.J. Performance evaluation of side-by-side optically coupled monolithic LYSO crystals. *Med. Phys.* **2022**, *49*, 5616–5626. [CrossRef] [PubMed]
22. Vinke, R.; Levin, C.S. A method to achieve spatial linearity and uniform resolution at the edges of monolithic scintillation crystal detectors. *Phys. Med. Biol.* **2014**, *59*, 2975. [CrossRef] [PubMed]
23. Morrocchi, M.; Hunter, W.; Del Guerra, A.; Lewellen, T.; Kinahan, P.; MacDonald, L.; Bisogni, M.G.; Miyaoka, R. Evaluation of event position reconstruction in monolithic crystals that are optically coupled. *Phys. Med. Biol.* **2016**, *61*, 8298. [CrossRef] [PubMed]
24. Worstell, W.; Doulas, S.; Johnson, O.; Lin, C.J. Scintillator crystal readout with wavelength-shifting optical fibers. In Proceedings of the 1994 IEEE Nuclear Science Symposium-NSS'94, Norfolk, VA, USA, 30 October–5 November 1994; Volume 4, pp. 1869–1873.
25. Worstell, W.; Johnson, O.; Zawarzin, V. Development of a high-resolution PET detector using LSO and wavelength-shifting fibers. In Proceedings of the 1995 IEEE Nuclear Science Symposium and Medical Imaging Conference Record, San Francisco, CA, USA, 21–28 October 1995; Volume 3, pp. 1756–1760.
26. Du, H.; Yang, Y.; Cherry, S.R. Comparison of four depth-encoding PET detector modules with wavelength shifting (WLS) and optical fiber read-out. *Phys. Med. Biol.* **2008**, *53*, 1829. [CrossRef]
27. An, S.J.; Kim, H.i.; Lee, C.Y.; Song, H.K.; Park, C.W.; Chung, Y.H. Design and simulation of depth-encoding PET detector using wavelength-shifting (WLS) fiber readout. *IEIE Trans. Smart Process. Comput.* **2015**, *4*, 305–310. [CrossRef]
28. Cargille. Optical Mounting Media—Meltmount, DATASHEET from. Available online: https://www.cargille.com/mounting-media/ (accessed on 9 December 2024).
29. Roncali, E.; Stockhoff, M.; Cherry, S.R. An integrated model of scintillator-reflector properties for advanced simulations of optical transport. *Phys. Med. Biol.* **2017**, *62*, 4811. [CrossRef]
30. Agostinelli, S.; Allison, J.; Amako, K.; Apostolakis, J.; Araujo, H.; Arce, P.; Asai, M.; Axen, D.; Banerjee, S.; Barrand, G.; et al. GEANT4 — A simulation toolkit. *Nucl. Instrum. Methods Phys. Res. Sect. A Accel. Spectrometers Detect. Assoc. Equip.* **2003**, *506*, 250–303. [CrossRef]
31. Geant4 Collaboration. *Book For Application Developers, Release 10.7*; CERN: Geneva, Switzerland, 2020.
32. Gumplinger, P. Optical Photon Processes in GEANT4. Users' Workshop at CERN, November 2002. Available online: https://geant4-internal.web.cern.ch/sites/default/files/geant4/support/training/users_workshop_2002/lectures/OpticalPhoton.pdf (accessed on 9 December 2024).

33. Hilger-Crystals. Guide to Selecting Inorganic Scintillator Crystals. Available online: https://www.hilger-crystals.co.uk/guide-to-selecting-inorganic-scintillator-crystals/ (accessed on 9 December 2024).
34. van der Laan, D.J.; Schaart, D.R.; Maas, M.C.; Beekman, F.J.; Bruyndonckx, P.; van Eijk, C.W. Optical simulation of monolithic scintillator detectors using GATE/GEANT4. *Phys. Med. Biol.* **2010**, *55*, 1659–1675. [CrossRef]
35. Luxium Solutions. 2024. Available online: https://luxiumsolutions.com/radiation-detection-scintillators/fibers (accessed on 9 December 2024).
36. Wanarak, C.; Chewpraditkul, W.; Phunpueok, A.; Kaewkhao, J. Luminescence and scintillation properties of Ce-doped LYSO and YSO crystals. *Adv. Mater. Res.* **2011**, *199*, 1796–1803. [CrossRef]
37. Wanarak, C.; Chewpraditkul, W.; Phunpueok, A. Light yield non-proportionality and energy resolution of Lu1. 8Y0. 2SiO5: Ce and LaCl3: Ce scintillation crystals. *Adv. Mater. Res.* **2011**, *284*, 2002–2007. [CrossRef]
38. Pidol, L.; Kahn-Harari, A.; Viana, B.; Virey, E.; Ferrand, B.; Dorenbos, P.; de Haas, J.T.; van Eijk, C.W. High efficiency of lutetium silicate scintillators, Ce-doped LPS, and LYSO crystals. *IEEE Trans. Nucl. Sci.* **2004**, *51*, 1084–1087. [CrossRef]
39. Mao, R.; Wu, C.; Lu, S. Crystal growth and scintillation properties of LSO and LYSO crystals. *J. Cryst. Growth* **2013**, *368*, 97–100. [CrossRef]
40. Vilardi, I.; Braem, A.; Chesi, E.; Ciocia, F.; Colonna, N.; Corsi, F.; Cusanno, F.; De Leo, R.; Dragone, A.; Garibaldi, F.; et al. Optimization of the effective light attenuation length of YAP: Ce and LYSO: Ce crystals for a novel geometrical PET concept. *Nucl. Instrum. Methods Phys. Res. Sect. A Accel. Spectrometers Detect. Assoc. Equip.* **2006**, *564*, 506–514. [CrossRef]
41. Georgadze, A.; Shivani, S.; Tayefi, K.A.; Moskal, P. Optimization of the WLS design for positron emission mammography and Total-Body J-PET systems. *Bio-Algorithms Med-Syst.* **2023**, *19*, 114–123. [CrossRef]
42. Brun, R.; Rademakers, F. ROOT—An object oriented data analysis framework. *Nucl. Instruments Methods Phys. Res. Sect. A Accel. Spectrometers Detect. Assoc. Equip.* **1997**, *389*, 81–86. [CrossRef]
43. Anger, H.O. Scintillation camera. *Rev. Sci. Instrum.* **1958**, *29*, 27–33. [CrossRef]
44. Zatcepin, A.; Pizzichemi, M.; Polesel, A.; Paganoni, M.; Auffray, E.; Ziegler, S.I.; Omidvari, N. Improving depth-of-interaction resolution in pixellated PET detectors using neural networks. *Phys. Med. Biol.* **2020**, *65*, 175017. [CrossRef]
45. Gong, K.; Berg, E.; Cherry, S.R.; Qi, J. Machine Learning in PET: From Photon Detection to Quantitative Image Reconstruction. *Proc. IEEE* **2020**, *108*, 51–68. [CrossRef]
46. Georgadze, A. Figures for the Feasibility Study of a PET Detector with Wavelength-Shifting Fiber Readout. *Mendeley Data* **2025**. [CrossRef]
47. Deng, Z.; Deng, Y.; Chen, G. Design and evaluation of LYSO/SiPM LIGHTENING PET detector with DTI sampling method. *Sensors* **2020**, *20*, 5820. [CrossRef]
48. Jones, T.; Townsend, D. History and future technical innovation in positron emission tomography. *J. Med. Imaging* **2017**, *4*, 011013. [CrossRef] [PubMed]
49. Xi, D.; Xie, Q.; Zhu, J.; Lin, L.; Niu, M.; Xiao, P.; Chen, C.T.; Kao, C.M. Optimization of the SiPM pixel size for a monolithic PET detector. *Phys. Procedia* **2012**, *37*, 1497–1503. [CrossRef]
50. Stockhoff, M.; Van Holen, R.; Vandenberghe, S. Optical simulation study on the spatial resolution of a thick monolithic PET detector. *Phys. Med. Biol.* **2019**, *64*, 195003. [CrossRef] [PubMed]
51. Cates, J.W.; Levin, C.S. Advances in coincidence time resolution for PET. *Phys. Med. Biol.* **2016**, *61*, 2255. [CrossRef]
52. Deng, Z.; Xie, Q.; Duan, Z.; Xiao, P. Scintillation event energy measurement via a pulse model based iterative deconvolution method. *Phys. Med. Biol.* **2013**, *58*, 7815. [CrossRef]